PHYSICAL REVIEW A VOLUME 48, NUMBER 6 DECEMBER 1993

Photoionization of the scandium atom. I. General features

F. Robicheaux* and Chris H. Greene
Department of Physics and Joint Institute for Laboratory Astrophysics, University of Colorado, Boulder, Colorado 80309-0440

(Received 1 April 1993)

In this paper we present the results of eigenchannel R-matrix calculations of the photoionization cross section of Sc from the $3d4s^2\,{}^2D_{3/2,5/2}$ ground electronic state. The calculations were performed in LS coupling using configuration interaction for the target states as well as for the full atomic wave function. The spin-orbit interaction was incorporated through a recoupling frame transformation. We focus on the gross dynamics of the atom that need to be described accurately to obtain good agreement with experiment.

PACS number(s): 32.80.Fb, 31.20.Di, 32.80.Dz

I. INTRODUCTION

The dynamics of transition-metal atoms has been studied both experimentally and theoretically in regimes where none of the electrons escapes to very large distances [1]. Relatively few experimental [2] or theoretical studies [3], however, have considered the transition metals in the autoionization region near the lowest few thresholds. The high melting points and low vapor pressures of these elements have hindered experimental studies, while the enormous number of channels has limited theoretical studies to close coupling calculations in LS coupling (or the use of hundreds of hours of CPU time on a Cray supercomputer). These types of calculations usually cannot achieve accuracy above the 10% level in the scattering parameters. The purpose of the calculations presented in this paper was to achieve accuracy of ∼1–2% in the scattering parameters and, more importantly, to show the level of accuracy achieved by different levels of approximation. The lessons learned from Sc may apply to other transition metals since the valence shells for all of these atoms include both s and d orbitals and the outer Rydberg electron will have p- or f-wave character.

We have completed an extensive study of Sc which will be presented in three parts. The main purpose of *this* paper is to explore the gross dynamics of Sc; we are especially interested in gaining a qualitative understanding of what determines the positions and shapes of various autoionizing resonances. In this paper, we present the spectra (convolved with an ~ 4 cm^{-1} FWHM weighting function) for photoionization from the ground electronic states $3d4s^2\,{}^2D_{3/2,5/2}$.

In the second paper [4] we will present classifications for most of the autoionizing states of Garton *et al.* [5] and a comparison of their lines with our unconvolved spectra. This comparison serves as a check of the accuracy of the theoretical spectra as well as a check on the experimental classifications. From this comparison we estimate the errors in quantum defects of unperturbed Rydberg series to be less than 0.03. The large number of lines that we were able to classify is the direct result of the accuracy of our calculations.

In the third paper (hereafter referred to as Paper III) [6], unconvolved spectra from the ground state $3d4s^2\,{}^2D_{3/2}$ and from the $3d^3\,{}^2_3D_{3/2}$ excited state (36 276.6 cm^{-1} above the ground state) will be presented with experimental photoionization spectra from the $3d^3\,{}^2_3D_{3/2}$ excited state; photoionization from the ground and excited states emphasizes different autoionizing states. It may be possible by comparing experimental and theoretical spectra from different initial states to unambiguously classify the bound and autoionizing states. The positions and classifications of ~ 100 new lines are reported and the classifications of several of the lines of the second paper are confirmed.

The calculations reported in these papers test for the first time whether the eigenchannel R-matrix calculations can reproduce the extremely complicated, intertwined spectra characteristic of the transition metals. It is not obvious that this, or any existing, theoretical approach can give spectroscopically useful information about the Sc spectrum. There are an order of magnitude more channels in the present calculation than in our previous calculations. It is possible, simply by going to higher energy, to arbitrarily increase the number of channels relevant to an experiment or calculation. For example, going to higher energy in Ba would require inclusion of the channels attached to the $6s$, $6p$, $5d$, $7s$, $7p$, $6d$, $4f$, ... thresholds in order to correctly describe the dynamics. However, the dipole operator does not couple the ground state strongly to states with two highly excited electrons. The spectra of the transition metals can be complicated near the very lowest thresholds. Since only one electron is being excited, the absorption can be quite strong. The following papers demonstrate the good agreement with the available experiments that we have achieved. In this paper we describe, in a general way, the origins of several of the striking features of the Sc spectrum; this presentation illustrates the possibility for a simple understanding of complex spectra.

II. SCANDIUM VITAL STATISTICS

A. Ionic (target) states

We are interested in photoionization from the Sc ground state which has the symmetry $3d4s^2\,{}^2D_{3/2}$. The threshold for ionization is 52 922 cm^{-1} $\sim$6.6 eV. Paper III gives another perspective on the Sc dynamics by examining the photoionization cross section from the $3d^3\,{}^2_3D_{3/2}$ state 36 276.63 cm^{-1} above the ground state; the photoionization dynamics can be probed from this state with a tunable laser although it takes two-photon absorption through an odd-parity excited state (e.g., the $4s^24p\,{}^2P^o_{1/2}$ state at 18 711.02 cm^{-1} above the ground state) to put a substantial fraction of atoms in the $3d^3$ state. The first 14 states of Sc$^+$ have even parity with the configurations $3d4s$, $3d^2$, and $4s^2$; the energies of these states [1] are given in Table I. Table I also shows the target (ionic) state energies calculated in LS coupling; these are discussed in Sec. IV. Notice that the first 13 levels have a spread of only 14 000 cm^{-1} $\sim$1.7 eV; the small spread is partly due to the near degeneracy of the $4s$ and $3d$ orbitals. The open p-shell atoms do not have their ionic levels spaced nearly this closely. The close spacing of ionic levels puts a large burden on the theory to produce accurate scattering parameters. Perturbers going to higher thresholds need to be at the correct energy or the levels that they perturb can have wildly different shapes and positions. The error in the energy of the perturber is $\Delta\mu/\nu^3$ (in atomic units) where $\Delta\mu$ is the error in the perturber's quantum defect and ν is the effective quantum number of the perturber attached to the higher threshold, $\nu = 1/\sqrt{2(I-E)}$. The error in the position of the perturber can be large (even if μ is accurate) when ν is small. Conversely, as ν gets larger the error in the energy decreases rapidly; for example, if the error in the quantum defect is 0.02 the error in the energy is $\sim$ 10 cm^{-1} for $\nu \simeq 7.6$ and $\sim$ 1 cm^{-1} for $\nu \simeq 16.4$.

The size of the errors in Table I raises questions about the ultimate accuracy of the full atomic calculation. These errors *do not* play a large role in the calculation for two reasons. First, the errors in the energies of the core states can be related to errors in a quantum defect through $\Delta\mu = \nu^3\Delta\varepsilon/Z^2$ where $\nu \sim 2.2$ and $Z = 2$; we find the errors in the quantum defects for these core states are less than $\sim$0.03. Second, we use the experimental values for the thresholds with the calculated short-range scattering parameters in the multichannel quantum defect theory (MQDT) calculation of the positions and widths of the *atomic* resonances; to determine the short-range scattering parameters we use the calculated core energies (the short-range scattering parameters do not depend strongly on energy and therefore the small shifts in energy from the calculated to the experimental thresholds do not have a large effect).

TABLE I. Experimental and theoretical Sc$^+$ energy levels.

	Energy (cm^{-1})	
Config.	Expt.	LS-averaged theor.
$3d4s\,{}^3D_1$	0.00	0
$3d4s\,{}^3D_2$	67.72	
$3d4s\,{}^3D_3$	177.76	
$3d4s\,{}^1D_2$	2540.95	1846
$3d^2\,{}^3F_2$	4802.87	3586
$3d^2\,{}^3F_3$	4883.57	
$3d^2\,{}^3F_4$	4987.79	
$3d^2\,{}^1D_2$	10944.56	13319
$4s^2\,{}^1S_0$	11736.36	10824
$3d^2\,{}^3P_1$	12074.10	12578
$3d^2\,{}^3P_2$	12101.50	
$3d^2\,{}^3P_3$	12154.42	
$3d^2\,{}^1G_4$	14261.32	15188
$3d^2\,{}^1S_0$	25955.2	27347

The odd-parity ionic states of the $3d4p$ type (from 26 000 cm^{-1} to 36 000 cm^{-1} above the $3d4s\,{}^3D$ ionic levels) play a role in the autoionization dynamics near the even parity thresholds; the $4s4p$ levels near 39 000 cm^{-1} and 56 000 cm^{-1} also play a role. The odd-parity target states are needed for a proper description of the polarizabilities of low-lying even-parity levels of Sc$^+$. The $3d4p5s$ and $4s4p4d$ states have energies slightly greater than those considered in this study; it is important for the convergence of the quantum defects that the theoretical energies and eigenvectors of these states be accurately reproduced. If we take the s-wave quantum defect to be $\sim$2.5 (which is a reasonable estimate from even parity s-wave Rydberg states), the $(3d4p)\,{}^1D^o5s$ state would be $\sim$10 000 cm^{-1} above threshold and very near the autoionizing region we examine in these papers.

B. Channels

A large number of open or "weakly closed" LS- and jj-coupled channels enter the calculation. The channels are constructed by attaching p and f waves onto the ionic levels in Table I. In LS coupling there are 2 ${}^2S^o$ channels, 11 ${}^2P^o$ channels, 11 ${}^2D^o$ channels, 13 ${}^2F^o$ channels, 8 ${}^2G^o$ channels, 2 ${}^4S^o$ channels, 4 ${}^4P^o$ channels, 6 ${}^4D^o$ channels, 5 ${}^4F^o$ channels, 4 ${}^4G^o$ channels, and 2 ${}^4H^o$ channels. In jj coupling there are 23 $J_f = 1^o/2$ channels, 37 $J_f = 3^o/2$ channels, 43 $J_f = 5^o/2$ channels, and 25 $J_f = 7^o/2$ channels. The notation $J_f = 7^o/2$, for instance, is shorthand for $J_f = \frac{7}{2}$, odd parity. As an example of the LS-coupled channels, the 11 ${}^2P^o$ channels are $(4s3d)^3D\varepsilon p$, $(4s3d)^1D\varepsilon p$, $(3d^2)^1D\varepsilon p$, $(4s^2)^1S\varepsilon p$, $(3d^2)^3P\varepsilon p$, $(3d^2)^1S\varepsilon p$, $(4s3d)^3D\varepsilon f$, $(4s3d)^1D\varepsilon f$, $(3d^2)^3F\varepsilon f$, $(3d^2)^1D\varepsilon f$, and $(3d^2)^1G\varepsilon f$. As an example of jj-coupled channels, the 9 $(3d^2)^3F_{J_c}$ channels with $J_f = 3^o/2$ are ${}^3F_2\varepsilon p_{1/2}$, ${}^3F_2\varepsilon p_{3/2}$, ${}^3F_3\varepsilon p_{3/2}$, ${}^3F_2\varepsilon f_{5/2}$, ${}^3F_2\varepsilon f_{7/2}$, ${}^3F_3\varepsilon f_{5/2}$, ${}^3F_3\varepsilon f_{7/2}$, ${}^3F_4\varepsilon f_{5/2}$, and ${}^3F_4\varepsilon f_{7/2}$.

Besides these channels, a large number of strongly closed channels have been included in the LS-coupled R-matrix calculation. These are channels whose basis functions all equal zero on the R-matrix surface. For example, for the ${}^2P^o$ symmetry there were basis functions of the type $(3d4p)^3F^ong$ where all of the ng orbitals go to zero on the boundary. Even though these channels are strongly closed, they are necessary for the level of convergence we have achieved. The strongly closed channels contributed roughly 2/5 of the basis functions. They were composed of all possible angular couplings of $(4s4p)ns, nd, ng$ and $(3d4p)ns, nd, ng$. For example, for the $^2P^o$ symmetry there were 14 strongly closed channels: $(4s4p)^{1,3}P^o ns$, $(4s4p)^{1,3}P^o nd$, $(3d4p)^{1,3}P^o ns$, $(3d4p)^{1,3}P^o nd$, $(3d4p)^{1,3}D^o nd$, $(3d4p)^{1,3}F^o nd$, and $(3d4p)^{1,3}F^o ng$.

III. THEORETICAL TECHNIQUES

A. Methodology

We employed the same theoretical methods described in our previous papers [7,8], numerically solving for the atomic dynamics using the streamlined formulation of the eigenchannel R-matrix procedure [9]. We used an R-matrix hypercubic volume having $\max\{r_1, r_2, r_3\} < 21$ a.u. in order to fit the four lowest ^2D levels within the R-matrix box. We calculated dipole matrix elements from three of these initial states to the continuum in order to gain different perspectives of the autoionizing states. We utilize a model Hamiltonian that treats the effects of the closed shell inner electrons on the valence electrons through a screening potential and a polarizability [10]. The three-electron Hamiltonian in atomic units is

$$\begin{aligned} H = {} & \sum_i H_V(\mathbf{p}_i, \mathbf{r}_i) + \sum_{\substack{i,j\\ i<j}} 1/r_{ij} \\ & -2\sum_{\substack{i,j\\ i<j}} P_1(\cos\theta_{ij})\sqrt{V_{\rm pol}(r_i)V_{\rm pol}(r_j)}, \end{aligned} \qquad (1)$$

where $\cos\theta_{ij} = \mathbf{r}_i \cdot \mathbf{r}_j / r_i r_j$. The computer code developed in Ref. [7] evaluates the angular part of the multielectron $1/r_{ij}$ matrix elements by summing products of 6-j coefficients and coefficients of fractional parentage. As in the previous calculations the atomic wave functions are fully antisymmetrized and have the orthonormality properties that are desirable for calculating many-electron matrix elements.

The one-electron Hamiltonian contains the interaction of each of the valence electrons with the nucleus and the inner core electrons and has the form

$$\begin{aligned} H_V(\mathbf{p}, \mathbf{r}) &= p^2/2 + V \\ &= p^2/2 - (3 + 18\exp\{-\alpha_1^l r\} \\ &\quad + \alpha_2^l r \exp\{-\alpha_3^l r\})/r + V_{\rm pol}(r). \end{aligned} \qquad (2)$$

Here $V_{\rm pol} = -\alpha_d[1 - \exp\{-(r/r_c)^3\}]^2/2r^4$ represents the interaction of an outer electron with the inner core arising from the core's dipole polarizability. We used the value of Ref. [11], $\alpha_d = 2.129$, for the dipole polarizability of the inner core of Sc^{3+}. The remaining parameters, α_i^l and r_c, were fitted to optimize agreement between the calculated energy levels of H_V and the experimental levels [1] of the 2+ ion [10]. We put a large weight on correctly fitting the spin-orbit splitting of the Sc^{2+} $3d$ level. By also fitting to the spin-orbit splitting, we obtain a better value for the matrix element $\langle nd|r^{-1}\partial V(r)/\partial r|nd\rangle$; this ensures a better shape for the Sc^{++} nd orbitals which should translate into a more physical potential. We list our values for α_i^l and r_c in Table II.

TABLE II. Parameters (in a.u.) for the semiempirical potential for the valence electrons.

l	α_1^l	α_2^l	α_3^l	r_c
0	3.17635	1.66883	1.67089	0.9
1	3.25751	1.80227	1.67268	0.9
2	3.40180	2.53291	1.40310	0.9
3-4	2.69890	1.04330	3.00830	0.9

Once we obtain the R matrix and the values of the wave functions at the surface, we can find the wave function everywhere outside of the volume by matching to Coulomb functions at the surface; the long range multipole interactions of the electron with the core are ignored because the phase shift caused by this interaction is much smaller than other errors in our procedure. At this point there are open and closed channels (the wave function diverges as $r \to \infty$ in the closed channels) in the calculation as is usual in multichannel quantum defect theory [12]. This part of the calculation is completely nonrelativistic; the K matrix and dipole matrix elements are in LS coupling. We calculated these parameters at 200 energies from -0.02 a.u. below the lowest ionization threshold to 0.07 a.u. above the lowest ionization threshold; we *linearly* interpolated the μ matrix and the $d/\sqrt{1+K^2}$ to obtain the K matrix and dipole matrix elements at intermediate energies [8,13].

The R-matrix part of the calculation was very fast. The total CPU time for all of the LS-coupled symmetries at 200 energies was about 22 CPU minutes on a DecStation 5200 computer.

In Sc, the thresholds are split as a result of the spin-orbit interaction. We incorporated this effect through the LS-jj frame transformation [12,14] which should work well because of the small spin-orbit splitting of Sc^+ ($\sim$100 cm^{-1}); the LS-jj frame transformation works well for Ba [10] which has spin-orbit splittings of the ion of $\sim$1000 cm^{-1}. The final cross sections and bound states are obtained by imposing the correct asymptotic boundary conditions in the open and closed channels; the wave function must satisfy the incoming-wave boundary condition in open channels and it must converge to zero in the closed channels. The rapid energy dependence of the scattering parameters near a Rydberg autoionizing state is a result of imposing the correct boundary conditions in the closed channels.

The spin-orbit interaction splits the energies of the states that only differ in their total angular momentum. It also causes an interaction between states with the same total angular momentum but different total spin or orbital angular momentum [for example, the $(3d^2)^1D_2$ state will interact with the $(3d^2)^3P_2$ state causing a mixing]. We have included the first interaction through the frame transformation. We have not included the mixing induced by the spin-orbit interaction because it has a negligible effect on the dynamics for Sc.

The final length and velocity gauge cross sections were calculated in jj coupling on a very fine energy mesh. There were 60 000 mesh points between the ^3D and ^3F thresholds and 40 000 mesh points between the ^3F and

^1G thresholds. The total CPU time to calculate the six different length and velocity gauge cross sections on this energy mesh was about 10 CPU hours on a DecStation 5200 computer. The large number of jj-coupled channels slowed this part of the calculation.

B. One-electron orbitals

We do not expand our many electron basis functions using the orbitals that are eigenstates of Eq. (2) because of the slow convergence; the R-matrix method uses a basis set expansion for describing the atomic dynamics, making it advantageous to use orbitals that are better suited to the problem [7,8]. We use orbitals that are better suited to the Sc^+ ion because they will converge the core states faster. Our $4s$, $4p$, and $3d$ orbitals were chosen to minimize the total energy of all the $4s^2$, $3d^2$, $4s3d$, $4s4p$, and $3d4p$ states [15]. Once these orbitals were fixed the $5s$, $5p$, and $4d$ orbitals were combined with the $4s$, $4p$, and $3d$ orbitals to construct two particle basis functions to help converge the $4s^2$, $3d^2$, $4s3d$, $4s4p$, and $3d4p$ states; the $5s$, $5p$, and $4d$ orbitals were chosen to minimize the total energy of these states. Basis functions that contained $6s$, $6p$, $5d$, or nf orbitals did not contribute more than ~1% to the two-particle wave functions and were not included in the target states.

Once we have determined the $4s$, $4p$, and $3d$ orbitals we construct a potential that has these orbitals as eigenstates. The form of the potential that we employ is [8]

$$\bar{V}_l(r) = V_l(r) + (1 - e^{-\bar{\alpha}_1^l r})/r + \bar{\alpha}_2^l (1 - e^{-\bar{\alpha}_3^l r})/r^2 . \quad (3)$$

We list the coefficients that we found to give the best values for the $4s$, $4p$, and $3d$ orbitals in Table III. The $5s$, $5p$, and $4d$ orbitals were constructed by superposing the orbitals for the potential of Eq. (3). For example, the $5s$ orbital was $0.80|5s\rangle - 0.35|6s\rangle + 0.29|7s\rangle - \cdots$ where the $|ns\rangle$ are the eigenstates of Eq. (3) that are zero at $r_0 = 21$ a.u.

In Fig. 1 we plot the Sc^+ $4s$ and $3d$ orbitals. The $3d$ orbital is much more compact than the $4s$ orbital. Since the $4s$ orbital does not screen the nucleus as effectively as the $3d$ orbital, it might be expected that the phase shift of $4s^2\varepsilon p$ waves will be larger than that for $3d4s\varepsilon p$ waves, which in turn will be larger than that for $3d^2\varepsilon p$ waves. In Fig. 2 we plot the zero energy radial p orbital for the (artificially) uncoupled $(4s^2)^1S\varepsilon p\,^2P^o$ channel, $(4s3d)^1D\varepsilon p\,^2P^o$ channel, and the $(3d^2)^1S\varepsilon p\,^2P^o$ channel [which has almost exactly the same phase shift as the $(3d^2)^1D\,\varepsilon p\,^2P^o$ channel]. Figure 2 bears out this expectation; a given node of an orbital moves closer to the origin as the phase shift increases. The quantum defects for these partial waves are $\mu = 1.82$ for the $(3d^2)^1S\varepsilon p\,^2P^o$ channel, $\mu = 1.88$ for the $(4s3d)^1D\varepsilon p\,^2P^o$ channel, and $\mu = 2.02$ for the $(4s^2)^1S\varepsilon p\,^2P^o$ channel. However, this expectation does not take into account exchange nor the other terms in the $1/r_{ij}$ interaction; the $(4s3d)^3D\varepsilon p\,^2P^o$ phase shift is larger than the $(3d^2)^3P\varepsilon p\,^2P^o$ phase shift but slightly smaller than the $(3d^2)^1S,^1D\varepsilon p\,^2P^o$ phase shifts. The f waves do not penetrate as far as the p waves and therefore the different screening of the $3d$ and $4s$ orbitals does not play a very strong role; interactions arising from the long range multipoles or the polarizability of the core can be more important. The first antinode of a zero energy f wave of Sc is near 10 a.u., which is very near the position of the first antinode of the zero energy hydrogenic f-wave orbital. The f-wave phase shifts of Sc are small but non-negligible, typically between 0.05π and 0.15π.

TABLE III. Parameters (in a.u.) for the potential for the natural orbitals.

l	$\bar{\alpha}_1^l$	$\bar{\alpha}_2^l$	$\bar{\alpha}_3^l$
0	0.10058	2.81709	0.70314
1	0.00000	3.81433	0.65828
2	0.86885	0.00000	0.00000
3-4	0.00000	0.00000	0.00000

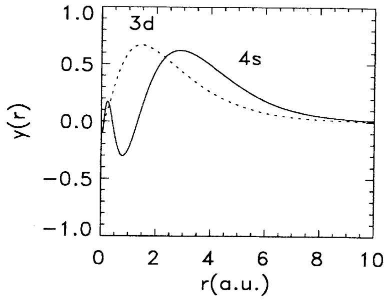

FIG. 1. The $4s$ (solid line) and $3d$ (dashed line) orbitals of Sc^+.

IV. CONSTRUCTING BASIS FUNCTIONS

In this section we describe the types of basis functions used for the ground and final state atomic wave functions; in Sec. V we describe the effect that leaving out some of the types of basis functions had on the calculated scattering parameters.

As in previous work we began the construction of the

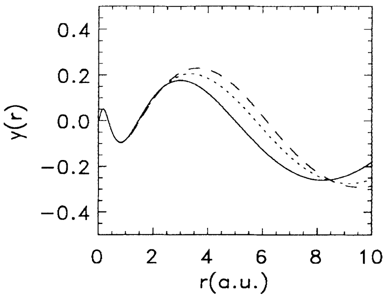

FIG. 2. The zero-energy p waves of Sc with different target states and $^2P^o$ final-state symmetry. The solid line is for the $(4s^2)^1S$ core, the dotted line is for the $(4s3d)^1D$ core, and the dashed line is for the $(3d^2)^1S$ core.

full atomic wave function by first assembling the basis functions needed to make the target (or ionic) wave functions. Where necessary we included configuration interaction in the target functions (e.g., the $4s^2$ state also contained $4p^2$ and $3d^2$ among other types of configurations) so that ~99% of each of the target states was represented. In choosing target basis functions we always try to work with the minimum number necessary to achieve convergence for the *atomic* dynamics because each target basis function translates to ~10 *atomic* basis functions.

The energies of the target states using this restricted basis set are given in Table I. The $(3d^2)^3P$, ^3F, and ^1G ionic states did not require any configuration interaction, in contrast to the other states. The calculated wave function for the ^3D state is $0.99|4s3d\rangle+0.14|4s4d\rangle$. The calculated wave function for the lowest ^1D state is $0.85|4s3d\rangle+0.14|4s4d\rangle+0.04|5s3d\rangle+0.51|3d^2\rangle-0.06|4p^2\rangle$; the calculated wave function for the next ^1D state is $0.49|4s3d\rangle+0.11|4s4d\rangle+0.09|5s3d\rangle-0.86|3d^2\rangle-0.11|4p^2\rangle$. These two ^1D eigenvectors do not agree with those obtained by Villemoes *et al.* [16] by fitting to the hyperfine levels of ^{45}Sc II. Their wave functions were very pure compared to ours; for example, one of their wave functions is $0.996|3d4s\ ^1D_2\rangle+0.076|3d^2\ ^1D_2\rangle-0.035|3d4s\ ^3D_2\rangle$. They included mixing arising from the spin-orbit interaction which we have ignored. We do not know why their eigenvectors are so pure; we expect large configuration interaction because of the near degeneracy of the $3d$ and $4s$ energies. The calculated wave function for the lowest energy ^1S state is $0.91|4s^2\rangle-0.37|3d^2\rangle+0.03|4d^2\rangle+0.08|3d4d\rangle+0.12|4p^2\rangle-0.09|4s5s\rangle-0.04|4p5p\rangle$; the calculated wave function for the next ^1S state is $0.34|4s^2\rangle+0.88|3d^2\rangle-0.12|4d^2\rangle-0.13|3d4d\rangle+0.24|4p^2\rangle+0.05|4s5s\rangle-0.12|4p5p\rangle$. The odd-parity target states had a similar level of mixing; we do not give their eigenvectors because they were not part of any open channels in this calculation.

As mentioned in Sec. III B, the orbitals were chosen to give the best overall convergence for the lowest even- and odd-parity target states; these are called the natural orbitals [15]. Some of the "configuration interaction" of the target states is caused by the difference in size and shape of the $3d$ and $4s$ natural orbitals used in the calculation from the $3d$ and $4s$ orbitals that give the best convergence for that state; for example, if we utilize the orbitals best suited for the ^3D target state, the largest mixing for that state would be ~0.1% of $4p4f$. This is over an order of magnitude smaller than the ~2% mixing of $4s3d$ when the wave functions were constructed from natural orbitals.

The odd-parity atomic basis functions were constructed by attaching p- and f-wave orbitals onto the even-parity target states and s-, d-, and g-wave orbitals onto the odd-parity target states; the even waves attached to the odd-parity target states were included to correctly describe the polarizability of the even Sc$^+$ levels. Also, near the higher even-parity thresholds are perturbers of the $3d4p5s$ and $3d4p4d$ types that need to be correctly described to converge the quantum defects. We attached p- and f-wave orbitals onto the odd-parity target states and s-, d-, and g-wave orbitals onto the even-parity target states to construct the even-parity initial states.

All of these wave functions are essentially close coupling type basis functions. We also included correlation type basis functions related to the close coupling type basis functions; for example, we included $4p^3$ basis functions because there were $4p^2\varepsilon p$ close coupling type basis functions in the calculation. The inclusion of correlation type basis functions influences the final result at the several percent level.

The ground state was calculated using extensive configuration interaction. The ground-state basis functions were constructed using the same principle described in the preceding paragraphs. These basis functions do not necessarily give the best convergence of the initial state; however, they do tend to give better agreement between the length and velocity gauge cross sections than basis functions that are indiscriminately chosen to give the best convergence for the ground state. It seems to be better to try to converge the initial and final state to the same level and in the same manner. Most of the ground-state basis functions describe relaxation of the orbitals due to the addition of the extra electron. The ground-state wave function (using the Sc$^+$ orbitals) is $0.91|(4s^2)^1S3d\rangle+0.24|(4s5s)^1S3d\rangle+0.08|4s(4p^2)^1D\rangle-0.16|4s(3d^2)^1D\rangle+0.21|3d(4p^2)^1S\rangle-0.08|(3d^3)^2_1D\rangle$ leaving out terms with amplitudes less than 0.07 in magnitude. If we use Sc orbitals the wave function is $0.95|(4s^2)^1S3d\rangle+0.08|4s(4p^2)^1D\rangle-0.17|4s(3d^2)^1D\rangle+0.21|3d(4p^2)^1S\rangle-0.08|(3d^3)^2_1D\rangle$ where $|\langle \mathrm{Sc}\ 4s|\mathrm{Sc}^+\ 4s\rangle|^2\sim 0.97$ and $|\langle \mathrm{Sc}\ 3d|\mathrm{Sc}^+\ 3d\rangle|^2\sim 0.997$. The nearly complete overlap of the Sc $3d$ orbital with the Sc$^+$ $3d$ orbital indicates the negligible relaxation of the $3d$ orbital after the photoionization. Relaxation of the $4s$ orbital, while small as well, is an order of magnitude larger.

V. CONVERGENCE TESTS

In Fig. 3 we present the results of a model calculation that shows the effect of including basis functions needed to describe the polarizability of the even parity ionic lev-

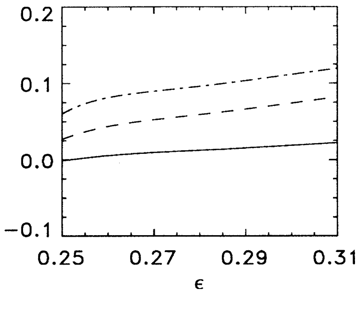

FIG. 3. The $4s^2\varepsilon f$ quantum defect as a function of energy in a.u. above the Sc ground state. The solid line is a single-channel calculation; the dashed line is a calculation which includes the $4s4p\ ^1Pnd$ basis functions; the dot-dashed line is a calculation which includes $4s4p\ ^1Pnd$ and ng basis functions.

els. The solid line shows the quantum defects of a one channel calculation with the channel being $4s^2\varepsilon f$; the quantum defect in this case is nearly zero. The dashed line shows the quantum defect obtained when closed basis functions of the $4s4p(^1P^o)nd$ type were included in the calculation; the quantum defect increases by ~0.05. The dot-dashed line shows the quantum defect when closed basis functions of the $4s4p(^1P^o)nd$ and ng types were included in the calculation; the quantum defect increases by another ~ 0.05. Not all of the channels are affected to this extent by the polarizability and some may be affected more strongly. This rather limited model calculation shows that the polarizability can affect the results at the 10% level (i.e., 0.1 in quantum defect). Therefore, channels with opposite parity target states may need to be included in calculations even if they are strongly closed.

In Fig. 4 we display the results of a two-channel model calculation which shows the effect of including configuration interaction in the description of the target states. The results are given in terms of the arctangents (divided by π) of the eigenvalues of the K matrix; the eigenvectors for the two different calculations were nearly identical. The continuum electron in both channels is an f-wave electron and the total symmetry of the atom is $^2F^o$; the two target states are $(3d4s)^1D$ and $(4s^2)^1S$. In the first calculation (solid line) the basis functions consisted of Hartree-Fock type target states. In the second calculation (dotted line) we included one extra configuration for each of the target states; the $(3d4s)^1D$ state became $a(3d4s)+\sqrt{1-a^2}(4d4s)^1D$ where $a^2 \simeq 0.96$ and the $(4s^2)^1S$ state became $a(4s)^2+\sqrt{1-a^2}(3d^2)^1S$ where $a^2 \simeq 0.83$. The main effect of this configuration interaction for these target states is to change the splitting of the quantum defects from ~0.07 to ~0.035 which implies a change by a factor of 4 in the small probability for scattering from the $^1S\varepsilon f$ channel into the $^1D\varepsilon f$ channel in one collision with the core. This calculation illustrates the importance of including configuration interaction in the target state even for f-wave continuum electrons which do not interact strongly with the core.

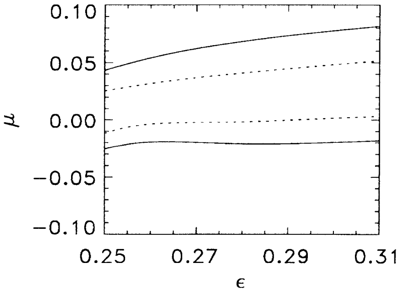

FIG. 4. The arctangents (divided by π) of the eigenvalues of the K matrix for a simple two-channel calculation. The solid lines are for single-term target states: $(3d4s)^1D\varepsilon f\ ^2F^o$ and $(4s^2)^1S\varepsilon f\ ^2F^o$. The dotted lines are for two-term target states: $(3d4s+4d4s)^1D\varepsilon f\ ^2F^o$ and $(4s^2+3d^2)^1S\varepsilon f\ ^2F^o$.

VI. RESULTS

In this section we discuss the origins of several of the features in the cross section. We do not discuss the detailed dynamics of individual lines; that analysis will be reported in the following paper.

A. Cross sections

In Fig. 5 we show a photograph of one of the plates of Garton *et al.* [5] together with a theoretical simulation of a plate using the averaged length gauge cross section; below these is a graph of the averaged length gauge cross section which is 0.4 times the $J_g = 3/2$ cross section plus 0.6 times the $J_g = 5/2$ cross section. We used a statistical mixture of $J_g = 3/2$ and $J_g = 5/2$ ground states to incorporate the thermal excitation of Sc in Ref. [5]; the temperature was near 2000 °C and the ground-state splitting is only 168.34 cm^{-1}. The simulated plate was constructed by experimenting with different relations between the darkness and the averaged cross section; cross sections less than 3 Mb were set to white and cross sections greater than 18 Mb were set to black to simulate saturation. It is clear from this figure that all of the major features lie close to the correct position. The theoretical widths of the lines are also in good agreement with the experiment, to the extent that one can compare them from inspection of the plates. This comparison is very encouraging since all of the strong features are states with small values for the effective quantum numbers; some of the features have ν as small as 5. For the classifications of the lines on this figure, see the discussion below on classifications, as well as the discussion of the classifications of the experimental lines marked on Fig. 1 of the following paper.

In Fig. 6 we show the averaged length gauge cross section and a reproduction of one of the plates between the ^1D and ^3F thresholds. This figure shows the difficulty introduced by the perturbing states in this region (see the individual cross sections in Fig. 7 for a clearer display of the perturbers). This figure also shows the difficulty introduced by having substantial populations in both of the ground states; the cross sections from the two different ground states are mixed to the extent that it is difficult to untangle the Rydberg series for each of the initial and final state symmetries. It is only through the experimental determination of which peaks belong to each of the ground states that the good agreement between the two becomes manifest.

In Figs. 7 and 8 we plot the six different length (solid line) and velocity (dashed line) gauge cross sections as a function of wavelength. These figures show the good agreement between length and velocity gauge that we have achieved. The $(4s3d)^3D$ ionization threshold is near 189 nm and the $(3d^2)^1G$ threshold is near 149 nm. The order of the cross sections is $3/2 \to 1^o/2$, $3/2 \to 3^o/2$, $3/2 \to 5^o/2$, $5/2 \to 3^o/2$, $5/2 \to 5^o/2$, and $5/2 \to 7^o/2$ from bottom to top. The cross section has been divided by a factor of 10 on two curves of Fig. 7 at the $(4s^2)^1S4f$ autoionizing state to fit it on the graph. The cross section

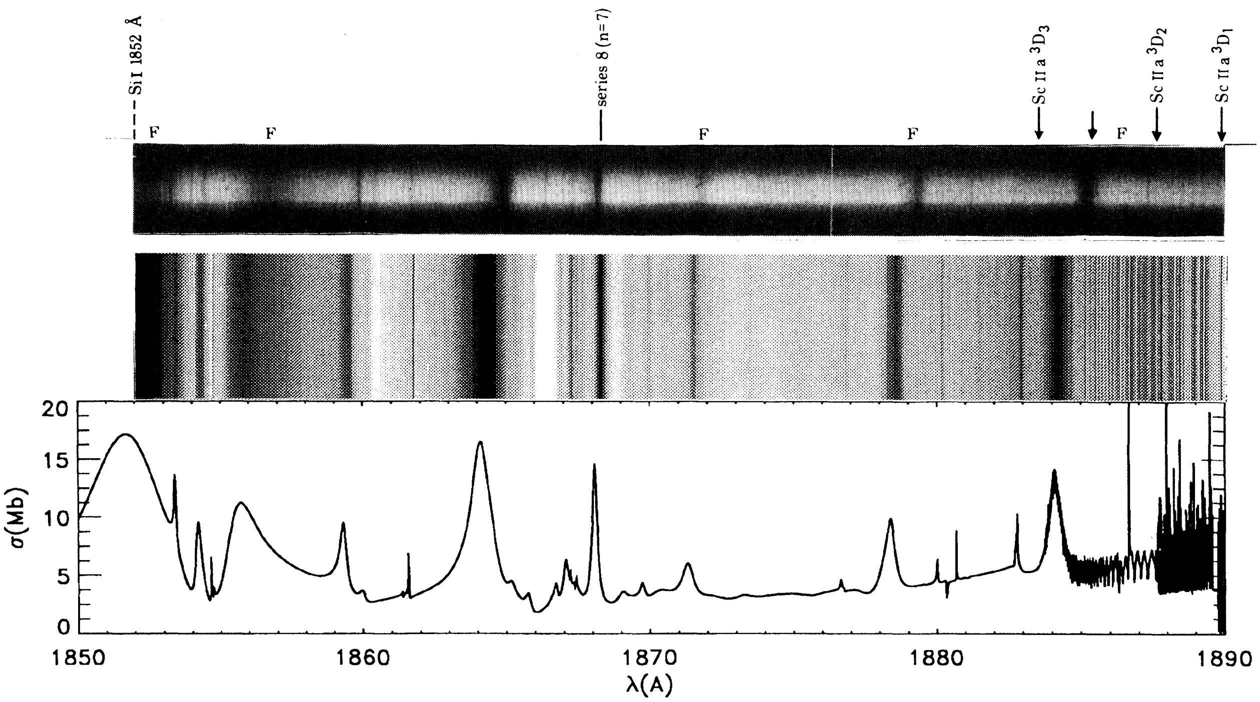

FIG. 5. Photograph (top) of one of the plates of Garton *et al.* [5] with a simulation (middle) of a plate using the theoretical cross section. Below these is the Sc photoionization cross section in the length gauge.

was convolved with a Gaussian weight function of width 2×10^{-5} a.u. ~ 4 cm^{-1} which suppresses sharp features with small oscillator strength. We have labeled some of the more prominent series for excitation from the $J_g = 3^o/2$ ground state.

Figure 7 gives the cross section from the $(4s3d)^3D$ thresholds near 189 nm to the $(3d^2)^3F$ thresholds near 173 nm. The $(4s3d)^1D$ threshold is near 181 nm. For the $3/2 \rightarrow 1^o/2$ cross section, the perturber marked with a "1" is the $(3d^2)^3P5p\ ^2P^o$ state, the series marked with a "2" is the $(4s3d)^1Dnp\,^2P^o$ Rydberg series, the line marked with a "3" is the $(3d^2)^1D4f\ ^2P^o$ state, and the

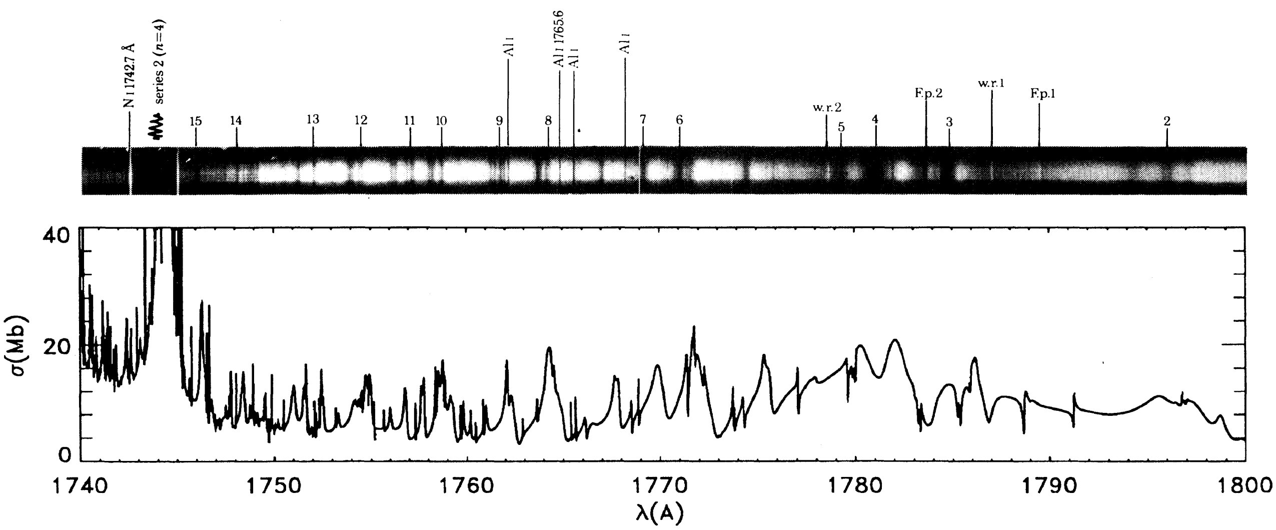

FIG. 6. Photograph of one of the plates of Garton *et al.* [5] with the theoretical cross section in the length gauge which illustrates the difficulties of disentangling the averaged spectrum near perturbers.

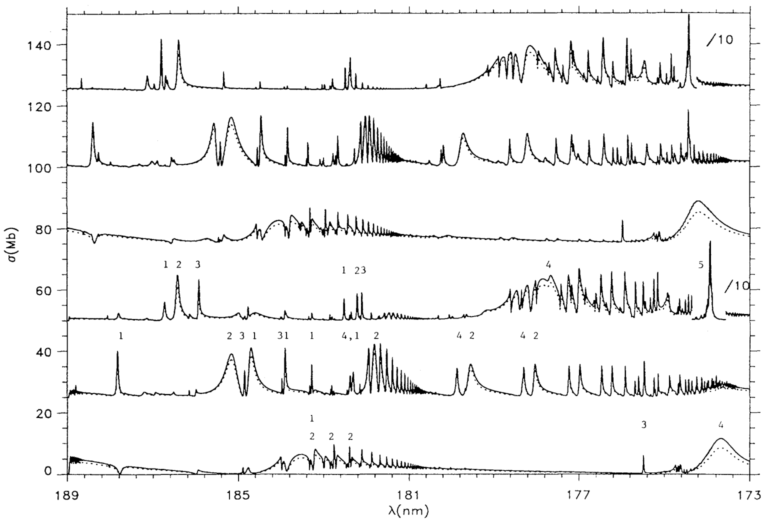

FIG. 7. The length (solid line) and velocity (dashed line) gauge cross sections for $^2D_{J_g} \rightarrow J_f^o$. We have added 25 Mb to the $3/2 \rightarrow 3^o/2$ cross section, 50 Mb to the $3/2 \rightarrow 5^o/2$ cross section, 75 Mb to the $5/2 \rightarrow 3^o/2$ cross section, 100 Mb to the $5/2 \rightarrow 5^o/2$ cross section, and 125 Mb to the $5/2 \rightarrow 7^o/2$ cross section. The $(4s^2)4f$ line has been divided by 10 in the $3/2 \rightarrow 5^o/2$ and $5/2 \rightarrow 7^o/2$ cross sections. The labels are discussed in the text.

"4" labels the $(4s^2)^1S6p\ ^2P^o$ state. For the $3/2 \rightarrow 3^o/2$ cross section, the states marked with a "1" are part of the $(4s3d)^1Dnp\ ^2D^o$ Rydberg series, the states labeled with a "2" and a "4" are mixtures of $(3d^2)^3Fnp\ ^2D^o$ and $^4D^o$ Rydberg series with the states marked "2" more nearly having $^2D^o$ symmetry (as the two series approach the $^3F_{J_c}$ spin-orbit split thresholds they become more strongly mixed until the series are best described in jj coupling), and the states marked with a "3" are part of the $(4s3d)^1Dnf\ ^2D^o$ Rydberg series. For the $3/2 \rightarrow 5^o/2$ cross section, the states marked with a "1" are part of a $(3d^2)^3F_2np$ Rydberg series, the states marked with a "2" are part of a $(3d^2)^3F_3np$ Rydberg series, the states marked with a "3" are part of the $(4s3d)^1Dnp\ ^2F^o$ Rydberg series, the perturber marked by the "4" is the $(3d^2)^1G5p\ ^2F^o$ state, and the "5" labels the $(4s^2)^1S4f\ ^2F^o$ state. The series attached to the $^3F_{J_c}$ thresholds are strongly mixed from the spin-orbit splitting of the thresholds. For example, the $J_f = 5^o/2\ ^3F_3np$ state at 182.2 nm is $0.61|^3F_38p_{3/2}\rangle + 0.48|^3F_38p_{1/2}\rangle+$ other states; the other states make up ~40% of the wave function.

Figure 8 gives the cross section from 172 nm, just above the $(3d^2)^3F$ thresholds, to near the $(3d^2)^1G$ threshold near 149 nm. From the 3/2 ground state, the ^3P thresholds are near 153.5 nm, the ^1S threshold is near 154.5 nm, and the ^1D threshold is near 156.5 nm. For the $3/2 \rightarrow 1^o/2$ cross section, the states marked with a "1" are part of the $(4s^2)^1Snp\ ^2P^o$ Rydberg series, the states marked by a "2" are part of the $(3d^2)^3Pnp\ ^2P^o$ Rydberg series, the state marked by the "3" is the $(3d^2)^1D5f\ ^2P^o$ state, and the states marked by a "4" are part of the $(3d^2)^1Dnp\ ^2P^o$ Rydberg series. There are no prominent $3/2 \rightarrow 3^o/2$ states in this region. For the $3/2 \rightarrow 5^o/2$ cross section the states marked with a "1" are part of the $(4s^2)^1Snf\ ^2F^o$ Rydberg series, the three states labeled with the "2" are $(3d^2)^3P_{J_c}5f$ states, the states marked by a "3" are part of the $(3d^2)^1Dnf\ ^2F^o$ Rydberg series,

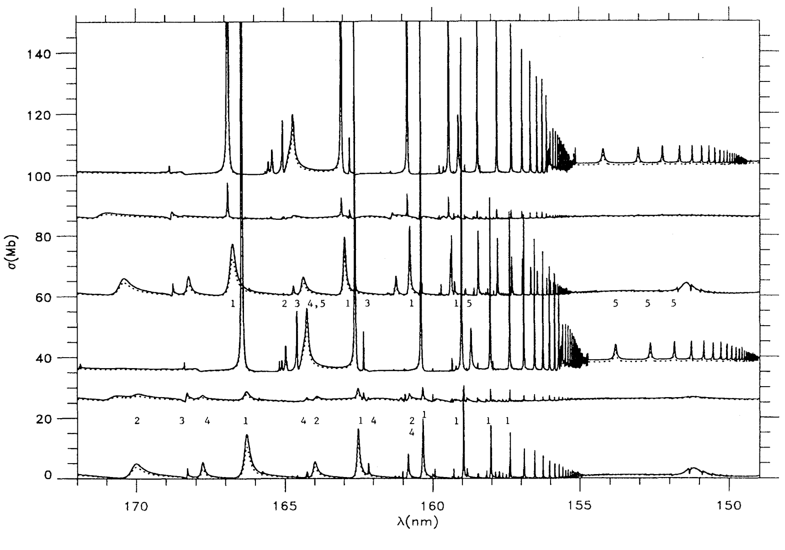

FIG. 8. Same as Fig. 7 except we have added 35 Mb to the $3/2 \rightarrow 5^o/2$ cross section, 60 Mb to the $5/2 \rightarrow 3^o/2$ cross section, 85 Mb to the $5/2 \rightarrow 5^o/2$ cross section, and 100 Mb to the $5/2 \rightarrow 7^o/2$ cross section.

the state labeled with the “4,5” is the sum of two peaks of $(3d^2)^1Dnp\ ^2F^o$ and $(3d^2)^1Gnp\ ^2F^o$ character, and the states labeled with a “5” are part of the $(3d^2)^1Gnp\ ^2F^o$ Rydberg series.

The calculated quantum defects of the $(4s^2)^1S21p\,^2P^o_{1/2}$, $(4s3d)^1D21p\,^2P^o_{1/2}$, and $(3d^2)^1D21p\,^2P^o_{1/2}$ states are 2.14, 1.91, and 1.97. From the discussion of Sec. III B we would expect the quantum defects to decrease from $(4s^2)^1S21p\,^2P^o$ to $(4s3d)^1D21p\,^2P^o$ to $(3d^2)^1D21p\,^2P^o$. However, the quantum defect for the $(4s3d)^1D21p\,^2P^o_{1/2}$ state is less than that for the $(3d^2)^1D21p\,^2P^o_{1/2}$ state because it is interacting with the $(3d^2)^3P5p\,^2P^o_{1/2}$ state of Fig. 7; the $^3P5p\,^2P^o$ state is lower in energy than the $(4s3d)^1D21p\,^2P^o$ state and therefore the interaction between the two states pushes the $21p$ state to higher energy, i.e., to smaller quantum defect. This comparison demonstrates that a simple analysis as in Sec. III B can help in understanding the dynamics underlying complicated spectra; however, the spectrum *is* complicated and the simple analysis may need modification for a fuller understanding.

In the range of Fig. 8, the spectra are dominated by the $(4s^2)nf$ resonances. The only other features apparent on the plates of Garton *et al.* [5] are from the $(3d^2)^1Gnp\ ^2F$ perturbers near 165 and 159 nm. This is not surprising since the $(4s^2)nf$ peaks are an order of magnitude larger than anything else in this energy range. The $(4s^2)np$ resonances possibly have enough oscillator strength to have been seen in the experiment; however, the calculated quantum defects for the two series differ by ~ 0.03 and therefore the two series are degenerate within the widths of the peaks. This explains the simplicity of the experimental spectrum in this energy range even though there are six thresholds.

One striking aspect of Figs. 7 and 8 is that almost every Rydberg series is perturbed. This derives from the large number of thresholds in a small energy range. Another interesting aspect of these figures is that some series derive most of their oscillator strength from perturbers, for example, in Fig. 7 the perturber labeled “1” in the $3/2 \to 1^o/2$ cross section and the perturber labeled “4” in the $3/2 \to 5^o/2$ cross section. This property of the spectra should serve as a warning: (a) to theorists because even though the calculated scattering parameters and dipole matrix elements may be accurate, low-n perturbers will have relatively large errors in their energy; the resulting calculated spectra may not resemble the experimental spectra; and (b) to experimentalists because the perturbed Rydberg series, which have rapidly changing quantum defects, may be more prominent than unperturbed series; the classification of the spectra can become problematical. The transition metals more complicated than Sc will be even harder to interpret for this reason.

B. Accuracy of the cross sections

Garton *et al.* [5] provided numerical values for the wavelengths of various autoionizing lines in their spectra. For several experimental lines we were able to unambiguously identify the corresponding theoretical line. From the difference in the energies we were able to estimate the errors in the theoretical scattering parameters. To estimate the errors we only utilized lines that were not perturbed by *low-n* autoionizing states because of the relatively large errors these perturbers can produce.

For the p-wave channels, we compared theoretical and experimental lines of $(4s3d)^1Dnp$, $(3d^2)^3F_{J_c}np$, and $(3d^2)^1Gnp$ character. From the lines of these different series, we found the largest errors in the p-wave quantum defects to be less than 0.03, with the errors of some series between 0.01 and 0.02. For the f-wave channels, we compared theoretical and experimental lines of $(4s^2)^1Snf$, $(3d^2)^3F_{J_c}nf$, and $(4s3d)^1Dnf$ character. From the lines of these different series, we found the largest errors in the f-wave quantum defects to be less than 0.02, with typical errors of 0.01.

This examination only reveals the errors in the quantum defects. It does not tell us anything about the errors in the widths of the resonances. The widths are related to the couplings of the resonances to the continua and give information on the off-diagonal S-matrix elements. Visual inspection of the plates in Ref. [5] shows that the great majority of calculated resonance widths are close to the experimental ones. The widths of the experimental lines reported in Paper III are very close to the theoretical widths. This gives us confidence that the errors in the S matrix are small.

C. Propensities

In LS coupling we would expect to see autoionizing lines appear in two different J_f symmetries where compatible with $|J_f - J_g| \leq 1$, $\Delta S = 0$, and $\Delta L \leq 1$. For example, a $^2D^o$ state should appear in both $^2D_{3/2} \to\ ^2D^o_{3/2}$ and $^2D_{3/2} \to\ ^2D^o_{5/2}$. Although it is true that the lines do tend to appear in two J_f symmetries, usually one of the J_f's has a much larger oscillator strength than the other. Two striking examples of this are the $4s^26p$ state near 173.8 nm that appears much more strongly in the $^2D_{3/2} \to\ ^2P^o_{1/2}$ channel than in the $^2D_{3/2} \to\ ^2P^o_{3/2}$ channel and the $4s^24f$ state near 174 nm that has over a factor of 10 more oscillator strength in the $^2D_{5/2} \to\ ^2F^o_{7/2}$ channel than in the $^2D_{5/2} \to\ ^2F^o_{5/2}$ channel. In the cases where there are two possible J_f, the propensities are (a) for the excitation to the $^2P^o$ symmetry, $3/2 \to 1^o/2$ dominates $3/2 \to 3^o/2$, (b) for the excitation to $^2D^o$ symmetry, $3/2 \to 3^o/2$ dominates $3/2 \to 5^o/2$ and $5/2 \to 5^o/2$ dominates $5/2 \to 3^o/2$, and (c) for excitation to $^2F^o$ symmetry, $5/2 \to 7^o/2$ dominates $5/2 \to 5^o/2$.

This propensity rule can be most easily understood by realizing that the favored transitions are simply those for which $\Delta J = \Delta L$. One expects this classically because the transition moment does not affect the spin vector. More quantitatively, in quantum mechanics the strength of a line depends on the square of its reduced dipole matrix element. This element is $d = \langle \gamma_g S_g L_g J_g || D^{(1)} || \gamma_f S_f L_f J_f \rangle$ and can be evaluated from Edmonds's [17] Eq. (7.1.8):

$$d = (-1)^{3/2+L_f+J_g}\sqrt{(2J_g+1)(2J_f+1)}\begin{Bmatrix} L_g & J_g & 1/2 \\ J_f & L_f & 1 \end{Bmatrix}\langle \gamma_g L_g||D^{(1)}||\gamma_f L_f\rangle, \tag{4}$$

where we have already substituted the values $S_g = S_f = 1/2$. This is a standard formula of atomic physics. As can be seen from Eq. (4), the only factors that depend on J_g and J_f are the square roots and the six-j coefficient. The six-j coefficient is simple enough that it can be evaluated analytically using Eqs. (6.3.3) and (6.3.4) of Ref. [17]. If $J_g = L_g - 1/2$, the ratio of the line strength in the $L_f - 1/2$ channel to that in the $L_f + 1/2$ channel is $(L_g+1)(2L_g-1)$ if $L_f = L_g$ and $(L_g-1)(2L_g+1)$ if $L_f = L_g-1$. This means the oscillator strength for ${}^2D_{3/2} \rightarrow {}^2D^o_{3/2}$ is nine times larger than that for ${}^2D_{3/2} \rightarrow {}^2D^o_{5/2}$ and the oscillator strength for ${}^2D_{3/2} \rightarrow {}^2P^o_{1/2}$ is five times larger than that for ${}^2D_{3/2} \rightarrow {}^2P^o_{3/2}$. If $J_g = L_g + 1/2$, the ratio of the line strength in the $L_f + 1/2$ channel to that in the $L_f - 1/2$ channel is $L_g(2L_g+3)$ if $L_f = L_g$ and $(L_g+2)(2L_g+1)$ if $L_f = L_g + 1$. This means the cross section for ${}^2D_{5/2} \rightarrow {}^2D^o_{3/2}$ is 14 times smaller than that for ${}^2D_{5/2} \rightarrow {}^2D^o_{5/2}$ and the oscillator strength for ${}^2D_{5/2} \rightarrow {}^2F^o_{5/2}$ is 20 times smaller than that for ${}^2D_{5/2} \rightarrow {}^2F^o_{7/2}$. If $J_g = L_g - 1/2$, it is much more probable to excite $J_f = L_f - 1/2$, and if $J_g = L_g + 1/2$, it is much more probable to excite $J_f = L_f + 1/2$. Again, all of these strong propensity-favored transitions obey the expected $\Delta J = \Delta L$ rule.

There is a striking bare spot in the $3/2 \rightarrow 1^o/2$ and $5/2 \rightarrow 3^o/2$ cross section on Fig. 7 which can be attributed to the same angular factor discussed in the preceding paragraph. Between $\lambda \sim 180$ and 174 nm, we would expect to see Rydberg series attached to the ${}^3F_{J_c}$ thresholds; these series would be jj coupled not LS coupled, and thus we might not expect the arguments of the preceding paragraph to apply. However, for $J_f = 1^o/2$ there is only one p-wave Rydberg series; it can be represented by the LS coupling ${}^3F\varepsilon p\,{}^4D^o_{1/2}$ or by the jj coupling ${}^3F_2\varepsilon p_{3/2}\ J_f = 1^o/2$. Since the quartet final state has zero dipole matrix element to the doublet ground state, the autoionizing states of this channel will not have oscillator strength. For the $5/2 \rightarrow 3^o/2$ cross section, the relevant jj-coupled channels are ${}^3F_2\varepsilon p_{1/2}$, ${}^3F_2\varepsilon p_{3/2}$, and ${}^3F_3\varepsilon p_{3/2}$ and are obtained by mixing the LS-coupled channels ${}^3F\varepsilon p\,{}^2D^o$, ${}^3F\varepsilon p\,{}^4D^o$, and ${}^3F\varepsilon p\,{}^4F^o$. However, the only channel that has a dipole coupling to the ground state (the ${}^2D^o$ channel) has its dipole matrix element reduced by a factor of $\sqrt{14}$ compared to the $5/2 \rightarrow 5^o/2$ channel which accounts for the lack of prominent autoionizing states in this energy range for this symmetry. We do not discuss the f-wave channels in this energy range because only the $4s^2\varepsilon f$ channel has a strong dipole coupling to the ground state compared to the p-wave channels.

The cross sections for $3/2 \rightarrow 3^o/2$ and for $5/2 \rightarrow 5^o/2$ in Fig. 8 do not have any prominent structures compared to the other cross sections. For these two cross sections most of the oscillator strength comes from the ${}^2D^o$ symmetry. However, the dipole matrix elements to the $(3d^2)^3P\varepsilon p$ and $(3d^2)^1D\varepsilon p$ channels for this symmetry are much smaller than for the other p-wave channels; the dipole matrix elements to the f-wave channels of this symmetry are also small. There is little direct excitation to the autoionizing series in this energy range for the ${}^2D^o$ and therefore no prominent autoionizing lines for these two cross sections. We do not have a simple explanation for why the dipole matrix elements to the $(3d^2)^3P\varepsilon p\,{}^2D^o$ and $(3d^2)^1D\varepsilon p\,{}^2D^o$ channels are so small.

D. Detailed analysis of a perturber

Figure 9 shows a blowup of a region of the unconvolved $J = 3/2 \rightarrow 3^o/2$ spectrum near a perturber plotted as a function of the effective quantum number; this graph covers the wavelength range $\sim$ 182.4–181.2 nm. This perturber can be classified as $(3d^2)^3F8p\,{}^2D^o_{3/2}$; the main effect of the perturber is felt by the $(3d4s)^1Dnp\,{}^2D^o_{3/2}$ Rydberg series. The sharp Rydberg series has the character $(3d4s)^1Dnf\,{}^2D^o_{3/2}$ and does not interact very strongly with the perturber. The quantum defect of a perturbed Rydberg series "increases" by 1 as the energy increases over the width of the perturber. Wang and Greene [18] showed that the widths of the lines in a three-channel perturbed Rydberg series trace out a Fano profile near a perturber; this means there should be an energy where the width goes to zero [19]. The line at $\nu = 13.96$ falls

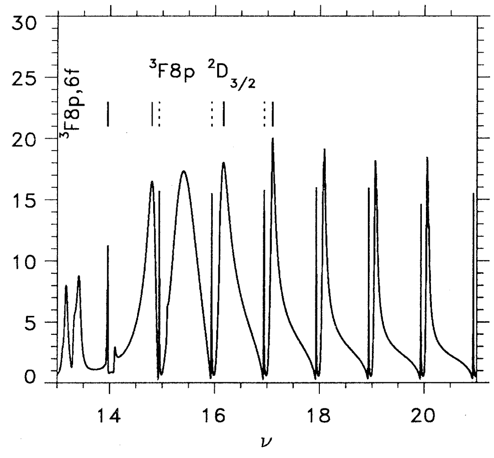

FIG. 9. The $J = 3/2 \rightarrow 3^o/2$ cross section as a function of the effective quantum number from the $(4s3d)^1D$ threshold. The states marked with solid vertical lines are $(4s3d)^1Dnp\,{}^2D^o$ autoionizing states and those marked with dotted vertical lines are $(4s3d)^1Dnf\,{}^2D^o$ autoionizing states. The quantum defect of the nf series is ~ 0.07 and the quantum defect of the *unperturbed np* series is ~ 2. The 14f and 16p states are degenerate within the widths of the states.

TABLE IV. The limited K matrix and dipole matrix (in a.u.) elements used to investigate Fig. 7. Channel 1 is ${}^3D\varepsilon p$, channel 2 is ${}^1D\varepsilon p$, and channel 3 is ${}^3F\varepsilon p$; all channels have ${}^2D^o$ total symmetry.

Chan.\Chan.	1	2	3
1	-0.24	-0.27	-0.49
2	-0.27	-0.16	-0.40
3	-0.49	-0.40	-0.96
d	3.9	3.3	5.8

very close to this energy and thus has a very narrow width.

Near a perturber the width and intensity of autoionizing lines usually change substantially over the width of the perturber; the widths of the autoionizing lines in Fig. 9 change fairly rapidly but the heights of the lines do not change very much. To discover the origin of this effect we examined the 3×3 block of the ${}^2D^o$ K matrix and the dipole matrix elements for the channels ${}^3D\varepsilon p$, ${}^1D\varepsilon p$, and ${}^3F\varepsilon p$; these parameters (near the ${}^1D$ threshold) are given in Table IV. With this limited set of parameters we recover a structure very similar to that in Fig. 9 but without the sharp ${}^1Dnf$ autoionizing states.

To obtain the cross section, channels 2 and 3 need to be closed off. This is shorthand terminology for imposing asymptotic boundary conditions in a closed MQDT channel. We will first close channel 3 and then close channel 2. When we close channel 3, we obtain a very energy dependent 2×2 K matrix and two energy dependent dipole matrix elements. Using Eqs. (2) of Ref. [18], we find $K_{11}(E) = -0.24(1+1/T_3)$, $K_{12}(E) = K_{21}(E) = -0.27(1+0.74/T_3)$, $K_{22}(E) = -0.16(1+1/T_3)$, $d_1(E) = 3.9(1+0.73/T_3)$, and $d_2(E) = 3.3(1+0.70/T_3)$ where $T_3 = K_{33} + \tan[\pi\nu_3(E)]$, with $\nu_3(E) = 1/\sqrt{2(I_3-E)}$ the effective quantum number for channel 3. [A zero width state would fall at energy $K_{12}(E) = 0$.] For a two channel problem the cross section is proportional to

$$\sigma \propto (d_1T_2 - K_{12}d_2)^2/[T_2^2 + (K_{11}T_2 - K_{12}K_{21})^2], \quad (5)$$

where $T_2 = K_{22}(E) + \tan[\pi\nu_2(E)]$. Resonances are near $T_2 = 0$ and therefore the heights of these resonances are $\sim [d_2(E)/K_{12}(E)]^2$. From the values of $K_{12}(E)$ and $d_2(E)$ given above, it is easy to see that the ratio is nearly constant and therefore the peak heights are nearly constant. A fortuitous and unusual combination of parameters was required to produce this unexpected constancy of individual resonance peak heights across the perturber.

E. Scattering probability matrix

In Table V we give the elements of the weakly energy-dependent scattering probability matrix for the ${}^2P^o$ symmetry near the $(3d^2)^3F$ thresholds. The element $|S_{ij}|^2$ of the scattering probability matrix is the probability for an electron in channel i to scatter into channel j during one collision with the core. If this number is relatively large for $i \neq j$, we say the channels i and j interact strongly; if it is relatively small we say the channels are weakly interacting. As expected, the f-wave channels hardly interact with other channels because f-wave electrons do not penetrate into the core region for Sc at this energy and therefore can only exert a weak force on the core. The p-wave channels display stronger interactions.

There are some exceptions. To understand the strength of the channel interactions we examined the $1/r_{12}$ matrix elements between the channels; for weakly interacting channels i and j, $\langle i|1/r_{12}|j\rangle$ will be small. For example, the $(3d4s)^1D\varepsilon p$ channel hardly interacts with the $(3d4s)^3D\varepsilon p$ channel. These channels only interact through exchange; the interaction when the $3d$ electron is the spectator is almost equal and opposite in sign to the interaction when the $4s$ electron is the spectator (when the $4s$ electron is the spectator the octupole interaction is larger than the dipole interaction). As another example, the $(3d4s)^1D\varepsilon p$ channel weakly interacts with the $(4s^2)^1S\varepsilon p$ channel; the direct quadrupole interaction is nearly equal and opposite in sign to the exchange dipole interaction. As a final example, the interaction between the $(4s^2)^1S\varepsilon p$ channel and the $(3d^2)^3P\varepsilon p$ channel is zero if these states are pure; only to the extent that $(3d^2)^1S$ mixes with the $(4s^2)^1S$ will there be an interaction between the $(4s^2)^1S\varepsilon p$ channel and the $(3d^2)^3P\varepsilon p$ channels.

VII. CONCLUSIONS

We have presented some of our theoretical results on the photoionization of Sc in the region near the low energy even-parity threshold states. We have tried to qual-

TABLE V. The scattering probability matrix for the ${}^2P^o$ symmetry near the $(3d^2)^3F$ thresholds. Channel 2 is $(4s3d)^1D\varepsilon p$, channel 5 is $(3d^2)^1D\varepsilon p$, and channel 7 is $(4s3d)^1D\varepsilon f$.

	${}^3D\varepsilon p$	${}^1D\varepsilon p$	${}^1S\varepsilon p$	${}^3P\varepsilon p$	${}^1D\varepsilon p$	${}^3D\varepsilon f$	${}^1D\varepsilon f$	${}^3F\varepsilon f$
${}^3D\varepsilon p$	0.351	0.001	0.258	0.206	0.146	0.019	0.019	0.002
${}^1D\varepsilon p$	0.001	0.832	0.011	0.072	0.040	0.031	0.007	0.006
${}^1S\varepsilon p$	0.258	0.011	0.625	0.014	0.035	0.043	0.007	0.008
${}^3P\varepsilon p$	0.206	0.072	0.014	0.582	0.043	0.047	0.018	0.018
${}^1D\varepsilon p$	0.146	0.040	0.035	0.043	0.701	0.007	0.001	0.027
${}^3D\varepsilon f$	0.019	0.031	0.043	0.047	0.007	0.838	0.001	0.015
${}^1D\varepsilon f$	0.019	0.007	0.007	0.018	0.001	0.001	0.946	0.001
${}^3F\varepsilon f$	0.002	0.006	0.008	0.018	0.027	0.015	0.001	0.924

itatively understand the dynamics of Sc through a discussion of some of the factors that affect the convergence of the scattering parameters, through a study of some of the propensities in the photoionization cross section, and through the classification of some of the prominent features in our spectra. We have also examined in detail the interaction of a perturber and a Rydberg series of autoionizing states.

Sc is the simplest transition metal. Almost every one of its Rydberg series is affected by a low-n perturbing state attached to a higher threshold. The other transition metals will also have this problem. The theoretical and experimental description of these elements in the autoionizing region will be a very difficult undertaking. Its solution should provide a new window on the interaction dynamics of several open shell atoms.

Despite the complexity of the spectra, the present calculations demonstrate that the underlying channel interaction dynamics (such as the scattering probability matrix) exhibit remarkable simplicity despite the inherent complexity of the spectra. Once the difficult task of attaining agreement between calculated and experimental spectra is completed, it is possible to continue the theoretical effort and untangle the origin of much of the dynamical complexity.

ACKNOWLEDGMENTS

This research is supported by the Division of Chemical Sciences, Office of Basic Energy Sciences, Office of Energy Research, U.S. Department of Energy Grant No. DE-FG-02-90ER14145.

---

* Present address: Department of Physics, Auburn University, Auburn, AL 36849-5311.

[1] J. Sugar and C. Corliss, J. Phys. Chem. Ref. Data **14**, Suppl. No. 2 (1985), and references therein.

[2] R.H. Page and C.S. Gudeman, J. Opt. Soc. Am. B **7**, 1761 (1990), and references therein.

[3] R.H.G. Reid, K. Bartschat, and P.G. Burke, J. Phys. B **25**, 3175 (1992); A.K. Pradhan and K.A. Berrington, *ibid.* **26**, 157 (1993), and references therein.

[4] F. Robicheaux and C.H. Greene, following paper, Phys. Rev. A **48**, 4441 (1993).

[5] W.R.S. Garton, E.M. Reeves, F.S. Tomkins, and B. Ercoli, Proc. R. Soc. London Ser. A **333**, 1 (1973).

[6] D. Armstrong and F. Robicheaux, this issue, Phys. Rev. A **48**, 4450 (1993).

[7] F. Robicheaux and C.H. Greene, Phys. Rev. A **46**, 3821 (1992); *ibid.* **47**, 1066 (1993).

[8] F. Robicheaux and C.H. Greene, Phys. Rev. A **47**, 4908 (1993).

[9] C.H. Greene and L. Kim, Phys. Rev. A **38**, 5953 (1988).

[10] C.H. Greene and M. Aymar, Phys. Rev. A **44**, 1773 (1991), and references therein.

[11] W. Johnson, D. Kolb, and K.-N. Huang, At. Data Nucl. Data Tables **28**, 333 (1983).

[12] U. Fano and A.R.P. Rau, *Atomic Collisions and Spectra* (Academic, Orlando, 1986); M.J. Seaton, Rep. Prog. Phys. **46**, 167 (1983).

[13] C.H. Greene and L. Kim, Phys. Rev. A **36**, 2706 (1987).

[14] A.R.P. Rau and U. Fano, Phys. Rev. A **4**, 1751 (1971); C.M. Lee and K.T. Lu, *ibid.* **8**, 1241 (1973).

[15] P.O. Löwdin, Phys. Rev. **97**, 1474 (1955); P.O. Löwdin and H. Shull, *ibid.* **101**, 1730 (1956); C. Froese-Fischer, J. Comput. Phys. **13**, 502 (1973).

[16] P. Villemoes, R. van Leeuwen, A. Arnesen, F. Heijkenskjöld, A. Kastberg, M.O. Larsson, and S.A. Kotochigova, Phys. Rev. A **45**, 6241 (1992).

[17] A.R. Edmonds, *Angular Momentum in Quantum Mechanics* (Princeton University Press, Princeton, NJ, 1974).

[18] Qiaoling Wang and C.H. Greene, Phys. Rev. A **44**, 1874 (1993).

[19] J.P. Connerade, in *Fundamental Processes in Atomic Dynamics*, Vol. 181 of *NATO Advanced Study Institute Series B: Physics*, edited by J.S. Briggs, H. Kleinpoppen, and H.O. Lutz (Plenum, New York, 1988), p. 565.

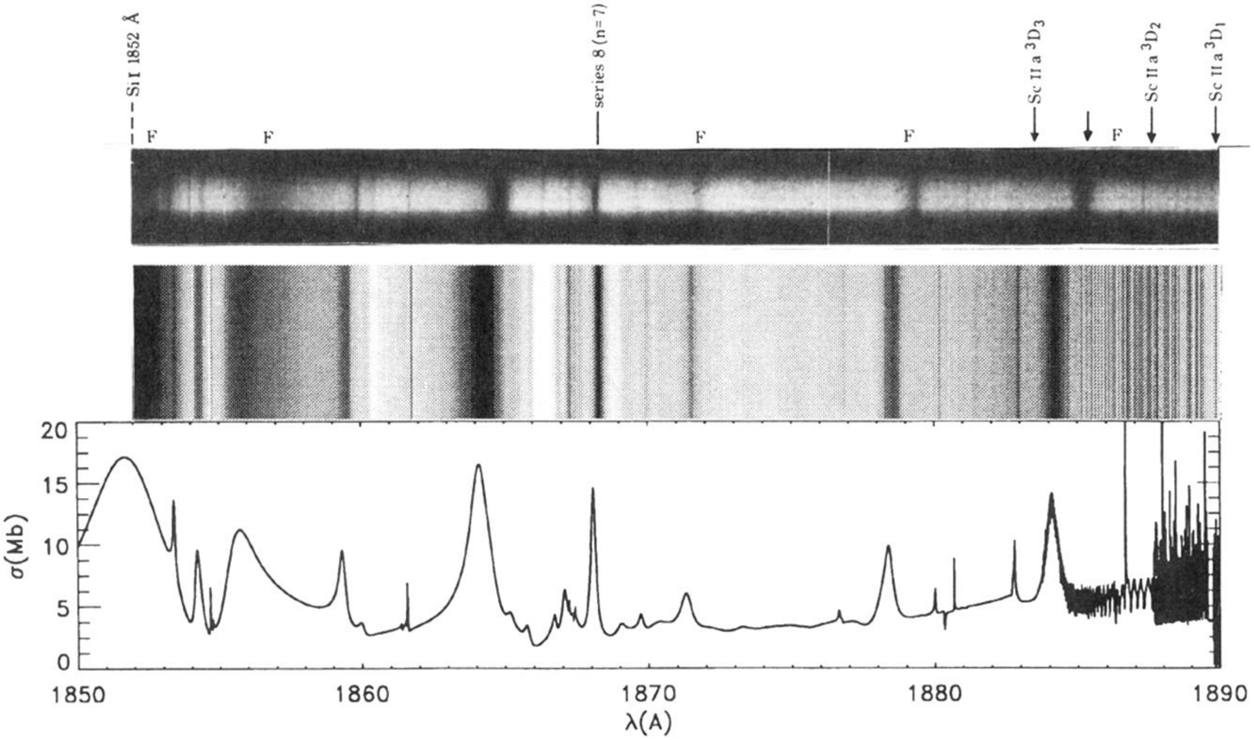

FIG. 5. Photograph (top) of one of the plates of Garton *et al.* [5] with a simulation (middle) of a plate using the theoretical cross section. Below these is the Sc photoionization cross section in the length gauge.

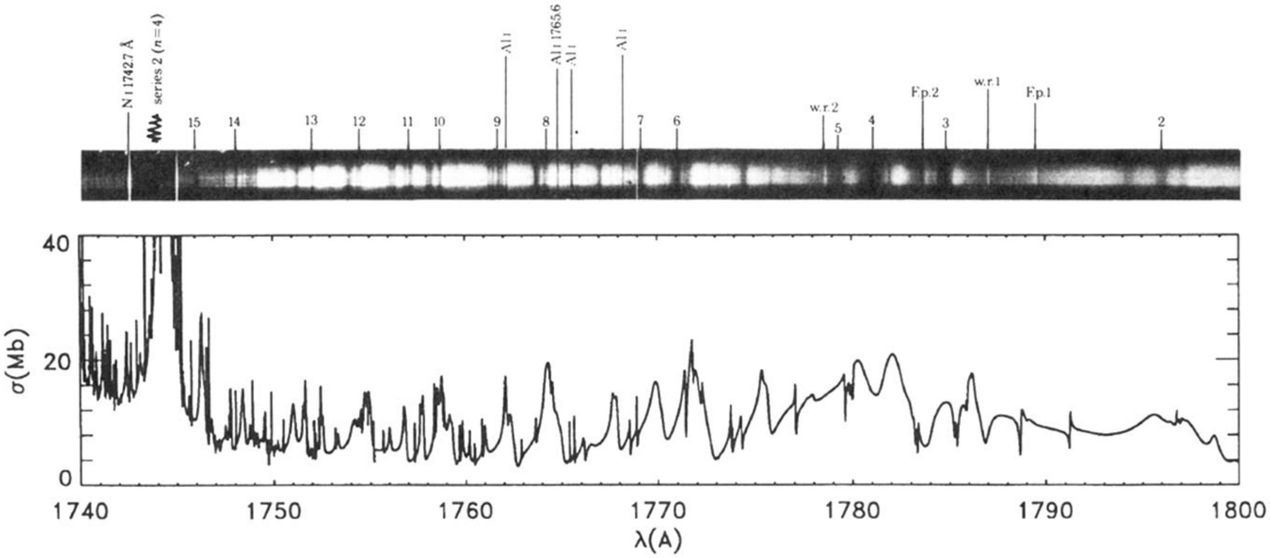

FIG. 6. Photograph of one of the plates of Garton *et al.* [5] with the theoretical cross section in the length gauge which illustrates the difficulties of disentangling the averaged spectrum near perturbers.